Accepted Manuscript

Optical nonlinearity in multiferroic bismuth ferrite

P. Nisha Francis, S. Dhanuskodi, M. Muneeswaran, Anitta Rose Thomas, N.V. Giridharan

PII: S0925-8388(16)32127-2

DOI: 10.1016/j.jallcom.2016.07.094

Reference: JALCOM 38262

To appear in: *Journal of Alloys and Compounds*

Received Date: 2 May 2016

Revised Date: 6 July 2016

Accepted Date: 8 July 2016

Please cite this article as: P.N. Francis, S. Dhanuskodi, M. Muneeswaran, A.R. Thomas, N.V. Giridharan, Optical nonlinearity in multiferroic bismuth ferrite, *Journal of Alloys and Compounds* (2016), doi: 10.1016/j.jallcom.2016.07.094.

Optical Nonlinearity in Multiferroic Bismuth Ferrite

P. Nisha Francis [1], *S. Dhanuskodi* [1,*], *M. Muneeswaran* [2],
Anitta Rose Thomas[3], *N. V. Giridharan* [2]

[1]*Nonlinear Optical Materials Laboratory, School of Physics, Bharathidasan University, Tiruchirappalli 620024, India.*

[2]*Department of Physics, National Institute of Technology, Tiruchirappalli Tamil Nadu 620015, India.*

[3]*Light and Matter Physics Group, Raman Research Institute, C.V. Raman Avenue, Sadashivanagar, Bangalore 560080, India.*

[*]Corresponding author E-mail: dhanus2k3@yahoo.com

GRAPHICAL ABSTRACT

Optical limiters based on multiferroic bismuth ferrite to limit high intensity laser pulses to protect optical sensors.

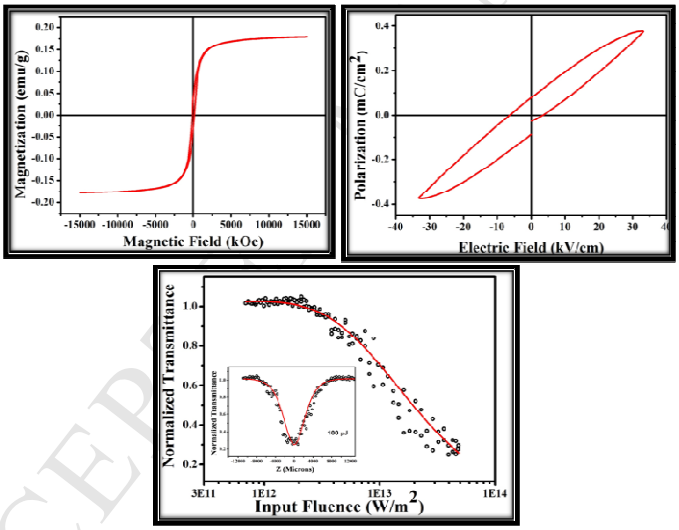

Optical Nonlinearity in Multiferroic Bismuth Ferrite

P. Nisha Francis [1], S. Dhanuskodi [1,], M. Muneeswaran [2],*
Anitta Rose Thomas[3], N. V. Giridharan [2]
[1]Nonlinear Optical Materials Laboratory, School of Physics, Bharathidasan University, Tiruchirappalli 620024, India.
[2]Department of Physics, National Institute of Technology, Tiruchirappalli Tamil Nadu 620015, India.
[3]Light and Matter Physics Group, Raman Research Institute, C.V. Raman Avenue, Sadashivanagar, Bangalore 560080, India.
*Corresponding author E-mail: *dhanus2k3@yahoo.com*

Abstract

Bismuth ferrite (BFO) nanoparticles were synthesized via sol-gel route with malic acid as a chelating agent. Structural characterization by XRD reveals the formation of single phase rhombohedral BFO and FTIR (433, 546 cm^{-1}) confirms the molecular structure. FESEM exhibits an agglomerated spherical morphology with an average particle size of 119 nm. The first and second order structural transitions have been detected at 821 (rhombohedral – orthorhombic) and 932° C (orthorhombic – cubic) by DTA. Strong visible light absorption with a band gap of 1.92 eV and defect related emissions at blue (417,450 nm) and green (521 nm) regions have been observed. Multiferroic properties at room temperature show weak ferromagnetism with remnant magnetization (M_r) 0.179 emu/gm and ferroelectric behavior with remnant polarization (P_r) 0.08 μC/cm^2. Dielectric measurements as a function of frequency (100 Hz - 5 MHz) and temperature (30 - 450° C) illustrate an evidence for magnetoelectric coupling with a peak at 350° C indicating the magnetic phase transition. Third order nonlinear optical property studied by the open aperture Z-scan technique (Nd: YAG, 532 nm, 5 ns) shows the reverse saturable absorption (RSA) based optical limiting behavior.

Keywords: Bismuth ferrite, Multiferroic, Ferromagnetism, Ferroelectricity, Z-scan, Optical limiting

1. Introduction

Bismuth ferrite, $BiFeO_3$, one of the very few multiferroics has attracted a great interest in recent years through the co-existence and interplay between ferroelectricity, ferroelasticity and ferromagnetism. The outstanding feature of BFO is that it is the only multiferroic compound known so far which undergoes phase transitions (ferroelectric to paraelectric at T_C =825° C and antiferromagnetic to paramagnetic at T_N = 370° C) [1]. Its ferroelectricity is driven by the steriochemically active lone pairs of Bi^{3+} ions causing a large relative displacement of Bi and O atoms along the pseudo-cubic [111] axis. The magnetic ordering is due to the spin canting which results in a small net magnetization leading to weak ferromagnetism in the antiferromagnetic substance. The control over the electric and magnetic ordering in BFO by the application of magnetic and electric fields respectively finds applications in spintronics [2] (as tunnel barriers in magnetic tunnel junctions and as exchange bias layers), nonvolatile memory devices [3] (with a 1.7V memory window of metal – ferroelectric – insulator – silicon structure) etc**.** Many potential and exciting properties such as gas sensing [4] (ethanol gas sensing with higher oxygen vacancy concentration) and photovoltaic [5] (perovskite intrinsic semiconductor sandwiched between p and n type layers forming p-i-n heterojunction) are observed in BFO depending upon the synthetic routes. Thus, most of the previous studies on BFO were focused on its multiferroic and linear optical properties. In this work, the nonlinear optical properties and optical limiting behavior of BFO is reported.

Recently, there is a growing interest for materials with second and third order nonlinearities as they found copious applications in opto-electronics. Second and third harmonic generation (SHG/THG) responses of $Bi_2ZnOB_2O_6$ single crystal studied by the Maker fringes technique show comparable efficiency with that of BBO and KDP [6]. A novel composite of same crystal with Ag nanoparticles embedded in PMMA polymer is also proposed for optoelectronic devices which is operated by SHG [7]. An organic- inorganic compound $Bi(III)I_5$ Iodobismuthate networks is found to be potential candidates for application in temperature controlled SHG switches like sensitive optical temperature detectors [8]. Nonlinearity arises when the material interacts with intense radiation and the nonlinear absorption i.e. change in transmittance of a material as a function of intensity or fluence can be saturable or reverse saturable one [9]. In the former, there will be an increase in transmittance with the increasing

incident intensity while in the latter the reverse occurs. Different effects resulting from this nonlinear absorption is employed in diverse areas covering large fields of photonic applications. Saturable absorbers are useful in mode locking, pulse compression and Q-switching while reverse saturable absorbers find applications in optical pulse processing like optical limiting and optical pulse shorteners [10]. Optical limiting in a material can be caused by the effects like excited state absorption (ESA), two or three photon absorption (2PA/3PA), free carrier absorption, etc. The open aperture (OA) Z-scan technique devised by Sheik-Bahae et al. [11] has been widely used for characterizing the third order optical nonlinearity. Following this technique, many reports are available for the nonlinear optical characteristics of metal oxide nanoparticles, nanocomposites and thin films. Lakshmi Reddy et al. [12] have described the 2PA with saturable absorption and optical limiting property of copper zinc aluminium ferrite by solid state reaction route. Reverse saturable absorption (RSA) based limiting behavior with 3PA in $NiFe_2O_4$ nanoparticles has been reported with nanosecond and femtosecond laser pulses [13]. Shiji Krishnan et al. [14] have investigated the two photon assisted exited state absorption in $YCrO_3$ multiferroic. The present work reports RSA based optical limiting in BFO when excited with Nd: YAG (532 nm, 5 ns) laser.

2. Experimental Procedure

BFO nanoparticles were synthesized by metal ions complexing with malic acid ($C_4H_6O_5$) by sol-gel method [15]. Nitrates of bismuth ($Bi(NO_3)_3.5H_2O$) and iron ($Fe(NO_3)_{3.}9H_2O$) precursors in 1:1 molar ratio (0.015M) were dissolved in distilled water and the solution was adjusted to a pH 1 by adding few drops of nitric acid (HNO_3). Malic acid solution with a molar ratio of 1:2 to the metal nitrates was prepared in distilled water by holding a hot plate of magnetic stirrer at 50° C. Metal nitrate precursor solution was poured slowly to this and the solution displayed yellow to orange colour after the addition of nitrates and turned brown upon further heating. Continuous heating at 80° C led to the evaporation of solvents and auto-ignition of the xerogel with the evolution of large quantities of brown fumes. The dark brownish powder obtained was ground well and calcined for two hours at 550° C to obtain well crystallized nanoparticles.

XRD was performed (RIGAKU, *Cu Kα*, λ=1.5406Å) to determine the crystalline phase and crystallite size. FTIR was recorded (JASCO 460 PLUS) by KBr pellet method. FESEM (FEI

QUANTUM FEG 200) along with EDS was employed to find out the morphology, particle size and elemental composition of the sample. The thermo gravimetric and differential analysis were carried out by TG/DTA (NETZSCH STA 449F3, upto 1000° C). UV-Visible (PERKIN ELMER LAMBDA 35) and emission (FLUOROMAX 4) spectra were recorded. Room temperature magnetic hysteresis loop was studied in a 7404 LAKESHORE vibrating sample magnetometer. Electrical properties were evaluated with a ferroelectric loop tracer (Radiant Technologies, USA) and an impedance phase analyzer (HIOKI 3535-50 LCR HITESTER) respectively. These were performed on 1 mm thick pellet of BFO nanoparticles coated with silver paste to serve as electrodes. To perform the Z-scan experiment, the second harmonic output from a Q-switched Nd: YAG laser (Minilite, Continuum, 532nm, 5ns) was used. Energy transmitted by the sample was measured using a pyroelectric energy probe (Rj7620, Laser Probe Inc.).

3. Results and Discussion

3.1 Structural Analysis

Fig.1 shows the XRD pattern of BFO calcined at 550° C for 2 hrs. Heating the powder at high temperature yields phase pure BFO with a perovskite structure and the pattern is in excellent accord with JCPDS file 86-1518 [15]. Structural analysis did not reveal any other parasitic phase related to the formation of impurity phases of bismuth ferric oxide such as $Bi_2Fe_4O_9$, $Bi_{25}FeO_{40}$ or Bi_2O_3 or Fe_2O_3. Sharp diffraction peaks are observed reflecting the greater crystallization of BFO. All the diffraction peaks are indexed to rhombohedral structure with lattice parameters a= 5.580 and c= 13.865 Å where as the standard values are a=5.578 and c= 13.862 Å. The average crystallite size D (35 nm) is evaluated by Debye-Scherrer equation

$$D = \frac{0.94\lambda}{\beta \cos\theta} \qquad (1)$$

where λ is the wavelength of X-ray, β is the full width at the half maximum and θ is the diffraction angle.

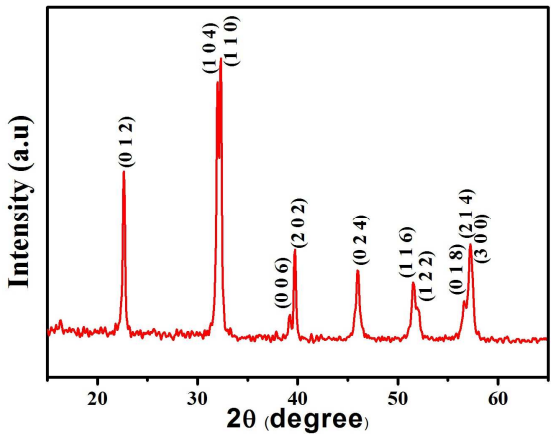

Fig.1 XRD pattern of BFO nanoparticles calcined at 500°C

The absorption features at 546 and 433 cm^{-1} are attributed to Fe-O stretching and bending vibrations respectively being the characteristics of the FeO_6 octahedral group in the perovskites (fig.2). Manisha Arora et al. [16] have specified that the peaks at 550 and 440 cm^{-1} are due to the overlapping of Fe-O and Bi-O vibrations. BiO_6 octahedral structure possesses peaks at 525 and 450 cm^{-1} due to the bending vibration of Bi-O. The small absorption bands at 3436 and 1620 cm^{-1} are assigned to O-H stretching and bending vibrations respectively. Also the weak bands at 880 and 1360 cm^{-1} are due to the existence of trapped nitrates on the surface [17, 18]. The morphology of BFO shows the spherical particles aggregated as clusters (fig.3) and the average particle size is found to be 119 nm. From the EDS spectrum given in fig.S1, the molar ratio of Bi: Fe is found to be ~1:1 in confirmation with the experimental procedure.

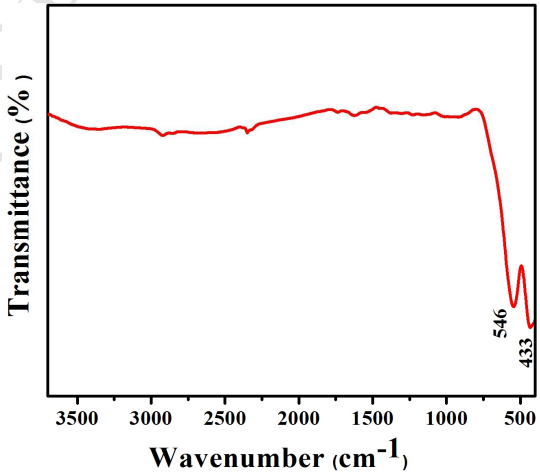

Fig.2 FTIR spectrum of BFO nanoparticles

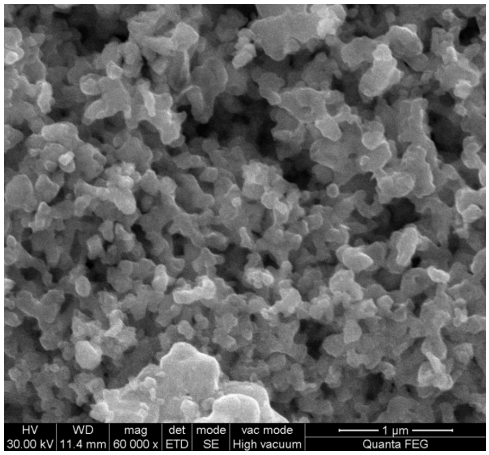

Fig.3 FESEM image of BFO nanoparticles

3.2 UV-Vis absorption and fluorescence spectra

Linear absorption spectrum taken for the concentration of 10 mg/ml of BFO is given in fig.4(a) and it reveals an absorption maximum at 454 nm. By calculating the absorption coefficient, the bandgap is found from the $(\alpha hv)^2$ vs hv plot as ~1.92 eV consistent with literature [18], where as the reported values are 2.12 eV (microcubes) [19] or 2.75 eV (thin films)[20]. Fluorescence (FL) spectrum of BFO for an excitation wavelength of 330 nm at room temperature is given in fig.4(b). Xuelian Yu et al. have pointed out that the FL spectrum of pure BFO shows only a blue emission at 454 nm (2.7 eV) due to self activated centers arising from lattice defects like vacancies and after Mn doping, a weak green emission at 518 nm is obtained [21]. Three principal emissions, one near band edge emission at 485 nm, a weak emission at 529 nm originated by defects at grain boundaries and a green emission at 545 nm due to oxygen vacancies are discussed for BFO nanotubes for an excitation wavelength of 400 nm [22]. A band-to-band transition at 460 nm and an oxygen vacancy related weak hump at 508 nm are observed for BFO ceramics [23]. But in the prevailing trial, a weak green emission at 521 nm (2.38 eV) along with two blue emissions at 417 (2.97 eV) and 450 nm (2.76 eV) are defect related ones, disclosing a new freedom in nanoscale optical applications.

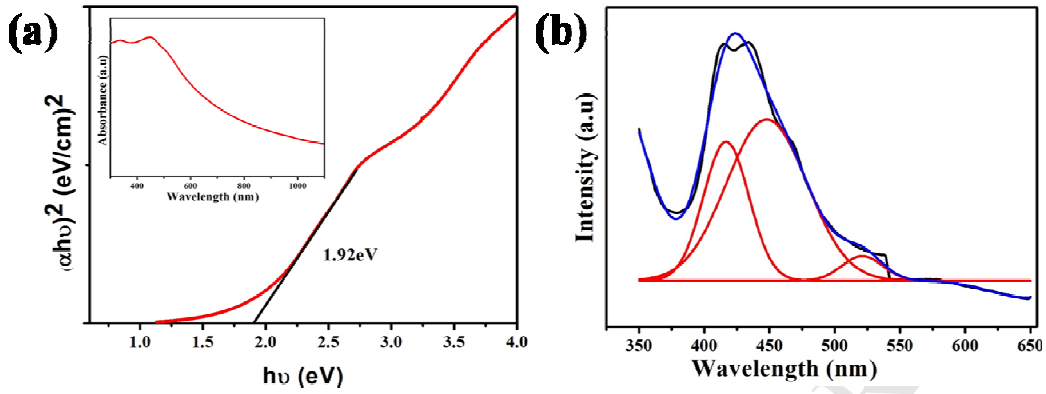

Fig.4(a) Tauc's plot and absorption spectrum (inset) and **(b)** fluorescence emission spectrum of BFO nanoparticles

3.3 Thermal Analysis

To investigate the thermal behavior of the calcined sample, TG-DTA has been carried out (fig.5). The TGA curve shows only a small weight loss (1.7 %) and there is no extra impurities present for further decomposition. From the curve, it is confirmed that the crystallization of BFO occurs at 450° C which is a criterion for selecting the temperature for calcination (550° C). A small weight loss in the temperature range from 0 to 400° C is due to dehydration of the precursors and the decomposition of nitrates. In the phase diagram of BFO, the first order ferroelectric to paraelectric transition (rhombohedral – orthorhombic) at 825° C and the second order transition (orthorhombic – cubic) at 931° C have been reported [1]. In the present observation, the T_C is 821° C and an exothermic peak at 932° C corresponding to the second order transition is also found. The first order transition is also accompanied by a volume contraction as evidenced from the TGA curve. Above 940° C, BFO is very unstable and it quickly disintegrates into parasitic phases such as $Bi_2Fe_4O_9$ and liquid Bi_2O_3. The weight loss after second order transition indicates the loss of Bi_2O_3 through sublimation process.

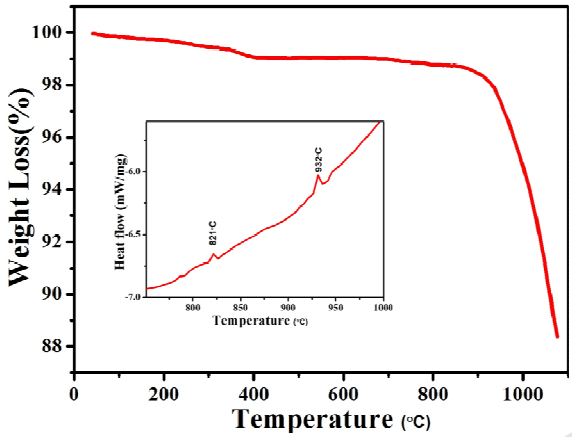

Fig.5 TGA curve of BFO nanoparticles calcined at 500°C and inset shows the DTA pattern

3.4 Multiferroism

To investigate the room temperature magnetic properties of BFO nanoparticles, magnetic measurements were performed. Magnetic hysteresis loop illustrated in fig.6 confirms a net magnetization at 300K and as expected for G-type antiferromagnetic materials, saturation in hysteresis loop is not attained. Though bulk BFO is antiferromagnetic, a ferromagnetic ordering is found in nanosized BFO resulting from the canted spin arrangement followed by suppression of helical structure [24]. The origin of magnetism is imputed to two possible reasons: 1) due to incomplete antiferromagnetic spin spiral or 2) due to uncompensated surface spins. Incomplete spin spiral is recounted to the particle size while uncompensated surface spins are related to the presence of defects. For a particle size of 50 nm and an applied field of 22 kOe, magnetic ordering has been reported because of the presence of residual magnetic moment by the uncompensated spins on the surface and thus breaking the cycloid spin structure [25]. Enhanced antiferromagnetic properties of BFO prepared by coprecipitation method have been reported with particle size in 50-100 nm range [26]. The enhancement of M_r is conferred by Rajasree Das et al. for Pr and Cr codoped BFO nanotubes having outer diameter of 250 nm and wall thickness of 50 nm [27]. Apart from this, an increase in superparamagnetism aroused from the statistical distribution of Fe^{3+} and Ni^{3+} in the octahedra or due to the creation of lattice defects is found in $BiFe_{1-x}Ni_xO_3$ [28]. As evidenced from XRD and FL, the ferromagnetic behavior exhibited by present BFO is featured to the collective effects of lower particle size thus interrupting the antiferromagnetic order and presence of vacancies related to the uncompensated surface spins.

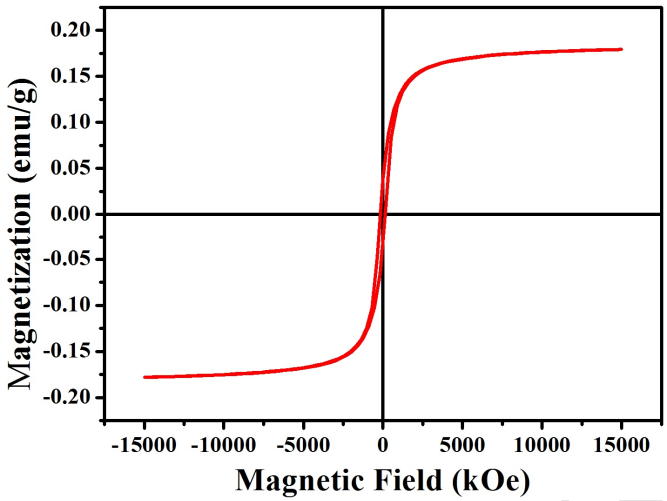

Fig.6 M - H hysteresis curve of BFO nanoparticles at room temperature

Polarization – electric field hysteresis loop of BFO at room temperature is depicted in fig.7. Because of the repulsion of Bi $6s^2$ lone pair of electrons, there arises a relative displacements of Bi and O ions resulting in net polarization. Even though the high leakage current is an implicit problem in BFO, the P-E loop displayed under an external ac field of frequency 10 Hz and strength ±10 kV/cm is an indirect indication of reduction in it. It is also observed that for the given field, the P – E loop is not fully saturated though there is a minimization of leakage current. A breakdown field was observed above 3500 V and the sample did not provide any signal for further increase in voltage. In the present investigation, the obtained values of P_r and E_c are low, but reliable with existing literature [29]. However, comparatively low values of P_r (~ 9 and 7 μC/cm^2) have been discussed for $Ba_{0.1}Gd_{0.05}$BFO and $Ba_{0.05}Gd_{0.1}$BFO ceramics respectively [30].A well saturated hysteresis loop with very large P_r has been reported for undoped ($2P_r$ ~168 μC/cm^2) [31] and co-doped ($2P_r$ ~235 μC/cm^2) [32] BFO thin films. Also, P-E values, very comparable to single crystals but almost half of the reported values for ceramics have been gained by solid state reaction [33], but the particle size is in micrometer (5-10 μm). The obtained magnetic and ferroelectric parameters along with available literature are listed in table 1.

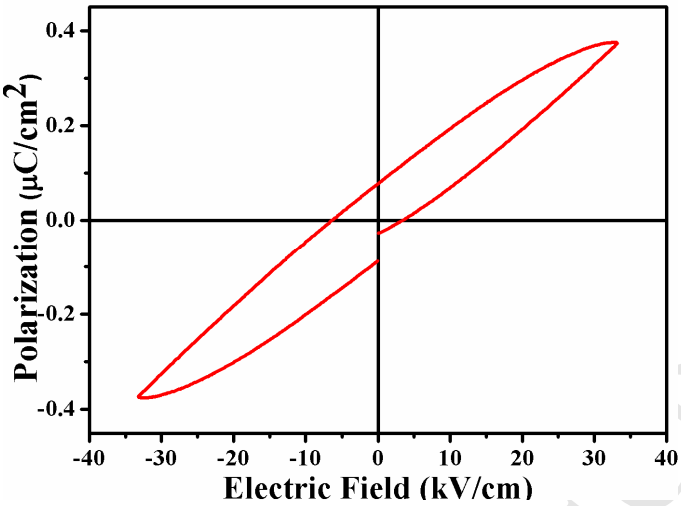

Fig.7 P - E loop of BFO nanoparticles at room temperature

Table 1: Comparison of room temperature ferromagnetic and ferroelectric parameters of BFO nanoparticles

Magnetic Parameters			**Ferroelectric Parameters**		
M_r **(emu/gm)**	H_c **(Oe)**	**Ref.**	P_r **(μC/cm^2)**	E_c **(kV/cm)**	**Ref.**
0.90	78	[21]	0.4	25	[25]
0.07	185	[25]	0.17	10	[29]
0.11	147	[26]	2.5	40	[33]
0.18	150	Present	0.08	5	Present

Frequency dependent (100 Hz – 5 MHz) dielectric measurement of BFO is carried out in the temperature range 30 to 450° C (fig.S2 (a and b)). Both dielectric constant (ε') and dielectric loss (ε'') increase with increasing temperature and a corresponding exponential decrease with increasing frequency is observed. This behaviour is explained on the basis of dipole relaxation indicating a large dispersion due to the Maxwell-Wagner type of interfacial polarization [16]. As oxygen deficiency is an inherent problem in BFO, as verified from the FL spectrum, space charge polarization is always present in it. Various polarizations such as electronic, atomic and ionic, dipolar and space charge or interfacial have contributions to the total polarization. Here, in

the low frequency range (~10^3 Hz) the interfacial polarization has much contribution thus inducing high values of ε' in that region. Dipolar polarization has effects only in the sub-infra red region (10^3 – 10^6 Hz) and it does not follow the electric field in the microwave region (10^8-10^{11} Hz) [30]. So, these participating mechanisms gradually decrease as the frequency increases and subsequently ε' decreases. This high frequency independence explains the incompetence of electric dipoles to be in pace with the applied field frequency. Frequency dependence of tan δ is interpreted with Koop's phenomenological theory [34]. High values of tan δ in the low frequency region are featured to the low leakage current because of the large insulating boundaries between the nanosize grains. Also there is a relaxation frequency accompanied by each polarization mechanism causing maximum dielectric loss. Nyquist plots of imaginary versus real impedance data as a function of temperature are shown in fig.8 (a). At low temperature and frequency, the impedance plot shows a straight line almost parallel to imaginary axis but at high values, it exhibits a semicircle. The semi circle is related to the grain interior resistance and the spike is attributed to the effect of blocking electrode [35]. Fig.8 (b) depicts the temperature dependence of ε' for different frequencies. A sudden jump in ε' at 350° C signifying the ferromagnetic to paramagnetic phase transition is observed at the proximity of T_N. In the case of magnetoelectrically ordered systems, this type of irregularity is predicted by the Landau – Devonshire theory of phase transition and it signifies the polarization-magnetization coupling [36].

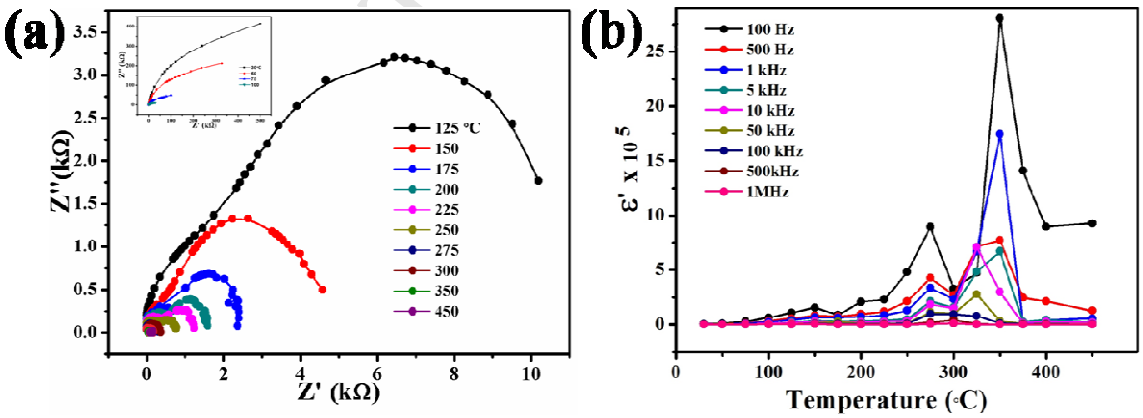

Fig.8 (a) Nyquist plot at 125 - 450° C (30 - 100° C in inset) and **(b)** Temperature dependent dielectric constant for BFO nanoparticles at various frequencies

3.5 Nonlinear absorption and optical limiting behavior

The sample for the Z-scan experiment was prepared by dispersing the nanoparticles in 0.03 g/ml concentration in ethylene glycol. To begin with, the experiment was performed for the solvent alone and it shows only a negligible absorption. The prepared nanoparticle solution taken in a 1 mm cuvette was irradiated by the second harmonic output of the Nd: YAG laser (532 nm, 5 ns, 10 Hz). The sample had a linear transmission of 70% and the direction of the laser beam (d = 3 mm) was fixed as Z-axis. By focusing the beam, which was spatially Gaussian, using a converging lens (f = 10 cm) and by translating the sample in the region near the focal point (z=0), the optical intensity seen by the sample can be varied. The transmittance as a function of sample position was measured for two input laser pulse energies of 50 and 100μJ. The nonlinear transmittance plotted against the sample position gives the open aperture Z-scan curve, from which the nonlinear absorption coefficient and optical limiting threshold are obtained.

Considering the nonlinear optical properties, there is a crucial distinction associated with the nonlinear absorption properties whether the photon energy of the laser field is greater than or smaller the band gap energy [37]. In the present work, the energy of the laser is greater than the bandgap of the material ($\hbar\omega$ (2.33 eV) > E_g (1.92 eV)). For this case, nonlinear response occurs as the result of band to band transitions resulting in an increase in conduction band electron density. The change in this electron concentration leads to several mechanisms like free-electron response, excited state absorption, plasma screening effects, band filling effects etc. resulting in a change in optical properties.

In general, the depth of the valley in the Z-scan experiment is a direct indication of the large excited state absorption compared to the ground state absorption, indicating the optical limiting efficiency of the materials [38]. Increase in the excited state population is an evidence for the increase in absorption with input fluence and the corresponding transmittance shows RSA characteristics. Since RSA involving two photons is numerically similar to two-photon absorption, the measured Z-scan data is numerically best-fitted to two-photon type absorption, given by the equation

$$T(z) = (1-R)^2 \frac{\exp(-\alpha L)}{\sqrt{\pi} q_0} \int_{-\infty}^{+\infty} \ln\left[1 + q_0 \exp(-x^2)\right] dx \qquad (2)$$

where *T(z)* is the normalized energy transmittance. Here, *L* and *R* are the sample length and surface reflectivity, respectively. It is known that when excited with nanosecond pulses, both excited singlet and/or triplet states have significant contribution to nonlinear absorption and is anticipated as saturable absorption along with effective two photon absorption. 2PA described by fourth rank polar tensors is related to the imaginary part of the third order nonlinear susceptibility $\chi^{(3)}$ and hence does not require non-centrosymmetry. Then the nonlinear absorption coefficient α is given by

$$\alpha(I) = \frac{\alpha_0}{1+\left(\frac{I}{I_s}\right)} + \beta I \qquad (3)$$

where *I* is the laser intensity, I_s is the saturation intensity and α_o is the unsaturated linear absorption coefficient of the sample. $q_0(z,t)$ is given by

$$q_0 = \beta(1-R)I_0 L_{eff} \qquad (4)$$

where I_0 is the peak on-axis intensity incident on the material and β is the effective 2PA coefficient, which characterizes the strength of nonlinear absorption. L_{eff} is given by

$$L_{eff} = \frac{1-\exp(-\alpha L)}{\alpha} \qquad (5)$$

The corresponding nonlinear propagation equation is given by

$$\frac{dI}{dz'} = -\left[\frac{\alpha_0}{1+\left(\frac{I}{I_s}\right)} + \beta I\right] I \qquad (6)$$

where *z'* is the distance of propagation within the sample. Fig.9 shows the measured Z-scan curves. Open circles denote the data points and solid curves are the best numerical fits. Limiting threshold is the input fluence at which the transmission decreases to 50 % of the linear transmission due to nonlinearity. The sample transmission versus input fluence plot for 100 μJ (which is the optical limiting curve, extracted from Z-scan data) is given in fig.10. Limiting

behavior for 50 μJ is provided in fig.S3. The obtained values of nonlinear absorption coefficient β, saturation intensity I_s and optical limiting threshold for 50 and 100 μJ and reported values of some spinel ferrites (532 nm, 5 ns, 0.2 Hz) are shown in table 2. It is known that thermally induced scattering reduces the transmitted energy when the sample is close to the beam focus. In the present case, this effect is not studied.

In the case of Bi doped ZnO thin films, RSA based optical limiting with β increasing from 1.02 to 5.76 x10^{-11} m/W for a Bi concentration of 1 to 5 at.% is attributed to the increased number of thermally agitated particles due to Bi concentration [39]. Dependence of surface roughness of these thin films on second and third order nonlinear susceptibilities is also studied by Abed et al.[40]. A switching from RSA to SA is found in EDT – TTF - Terpy ligand with Ru and Fe metal complexes using Nd: YVO_4 laser (532 nm, 30 ps, 10 Hz) due to the introduction of metal cations which change the energy levels of the system. The observed β is 0.64 x 10^{-10} m/W [41] which is comparable to the present study (0. 87 x 10^{-10} m/W). In perovskites, multiferroic $YCrO_3$ shows nonlinearity with a 3PA coefficient of 4.5 x 10^{-24} m^3/W^2 under the irradiation of nanosecond pulses [14]. The observed fifth order nonlinearity is considered as 2PA followed by ESA. El-Bey et al. [42] have observed 2PA and an enhancement of THG in multiferroic $Bi_2Fe_4O_9$ near antiferromagnetic phase transition by the application of an external magnetic field (0.3 T) and photoinduced power density (0.9 mJ/cm^2) due to magneto-electric coupling.

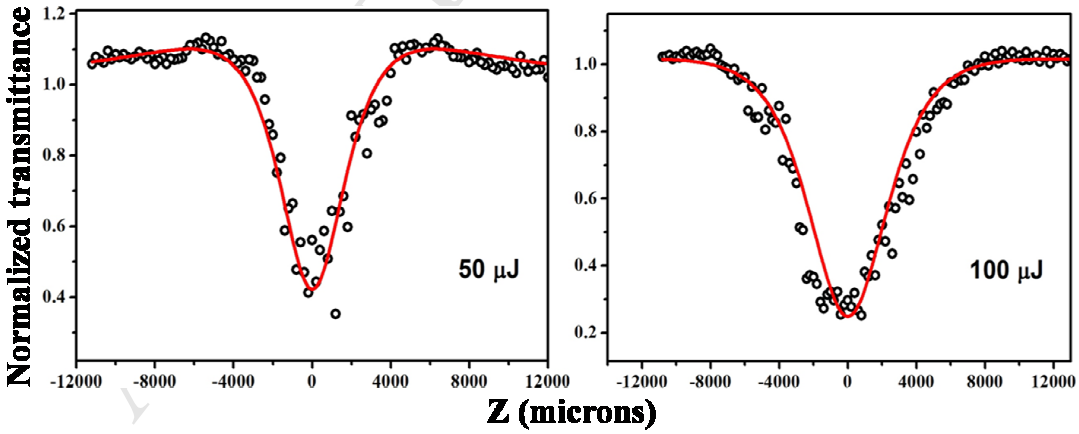

Fig.9 Z – scan curves of BFO nanoparticles for 50 and 100μJ

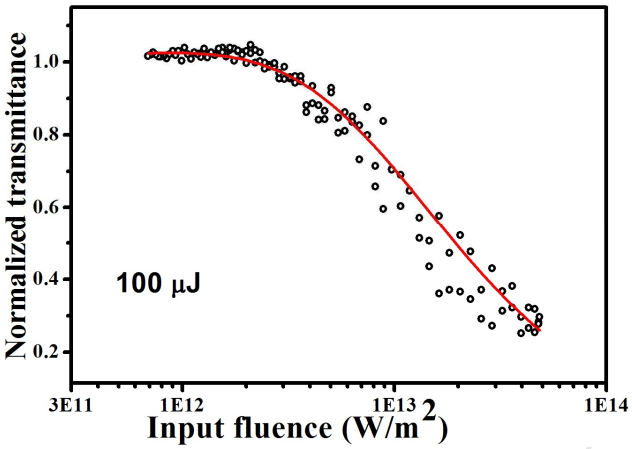

Fig.10 Optical limiting behavior of BFO nanoparticles, extracted from the Z-scan data.

Table 2: Effective 2PA coefficient, saturation intensity and limiting threshold for some ferrites.

Sample	Input Energy (μJ)	β ($\times 10^{-10}$ m/W)	I_s ($\times 10^{11}$ W/m^2)	Limiting Threshold (J/cm^2)	Ref.
$ZnFe_2O_4$	12	5	5	2.23	[38]
$NiZnFe_2O_4$	12	5.8	5	1.60	[38]
$CuZnFe_2O_4$	12	7.9	5.2	1.49	[38]
$BiFeO_3$	50	0.87	9.5	2.09	Present
$BiFeO_3$	100	0.89	22	1.94	Present

4. Conclusion

Using malic acid as chelating agent, BFO nanoparticles have been prepared by sol-gel method and TGA reveals the formation of BFO at 550° C. Powder XRD verifies the single phase rhombohedral structure with average crystallite size of 35 nm. FTIR reveals the overlapping of stretching (546 cm$^{-1)}$ and bending (433 cm^{-1}) vibrations of Bi-O and Fe-O bonds in BiO_6 and FeO_6 octahedral groups. The UV – Vis absorption spectrum signifies a much higher utilization of visible light with a direct band gap of 1.92 eV. In fluorescence spectrum, blue (417, 450 nm) and green (521 nm) defect related emissions indicate its potential applications in light emitting diodes. Ferroelectric to paraelectric transition at 821° C and orthorhombic to cubic structural

transition at 932° C are noticed in DTA. M-H loop shows ferromagnetism (M_r = 0.18 emu/gm) compared to the antiferromagnetic bulk resulting from the suppression of helical structure and the uncompensated surface spins due to defects. P-E loop specifies the ferroelectric behavior with incomplete hysteresis due to leakage current. An increase in both dielectric constant and loss with temperature lead to capacitor application of BFO and a ferromagnetic to paramagnetic phase transition at 350° C at the vicinity of T_N is observed. From the open aperture Z-scan measurements, BFO is found to exhibit nonlinear absorption (0.87×10^{-10} m/W) with a low limiting threshold (1.94 J/cm^2), making BFO an efficient optical limiter for the protection of optical sensors.

References:

1. Gustau Catalan, James F. Scott, Adv. Mater. **21 (**2009) 2463 - 2485.
2. H. Bea, M. Bibes, S. Cherifi, F. Nolting, B. Warot-Fonrose, S. Fusil, G. Herranz, C. Deranlot, E. Jacquet, K. Bouzehouane, A. Barthelemy, Appl. Phys. Lett. **89** (2006) 242114.
3. Pi-Chun Juan, Jyh-Liang Wang, Tsang-Yen Hsieh, Cheng-Li Lin, Chia-Ming Yang, Der-Chi Shye, Microelectron. Eng. **138 (**2015) 86 - 90.
4. Guangzhi Dong, Huiqing Fan, Hailin Tian, Jiawen Fang, Qiang Li, RSC Adv. **5** (2015) 29618 - 29623.
5. Soumyo Chatterjee, Abhijit Bera, Amlan J. Pal, Appl. Mater. Interfaces **6 (**2014) 20479 – 20486.
6. K. Iliopoulos, D. Kasprowicz, A. Majchrowski, E. Michalski, D. Gindre, B. Sahraoui, Appl. Phys. Lett. **103** (2013) 231103.
7. A. Majchrowski, A. Wojciechowski, L. R. Jaroszewicz, M. Chrunik, A. Fedorchuk, B. Sahraoui, I. V. Kityk, J. Mater. Sci.: Mater. Electron. **25** (2014) 2426 - 2434.
8. Wenhua Bi, Nicolas Louvain, Nicolas Mercier, Jerome Luc, Ileana Rau, François Kajzar, Bouchta Sahraoui, Adv. Mater. **2**0 (2008) 1013 - 1017.
9. R.L. Sutherland, Handbook of Nonlinear Optics, Marcel Dekker, New York (1996) Chapt.9.
10. Xiao-Fang Jiang, Lakshminarayana Polavarapu, Shu Ting Neo, T. Venkatesan, Qing-Hua Xu, J. Phys. Chem. Lett. **3** (2012) 785 - 790.
11. M. Sheik-Bahae, A. A. Said, E.W. Van Stryland, Opt. Lett. **14** (1989) 955 - 957.
12. S. Lakshmi Reddy, T. Ravindra Reddy, Nivya Roy, Reji Philip, Ovidio Almanza Montero,

Tamio Endo, Ray L. Frosy, Spectrochim. Acta Mol. Biomol. Spectros. **127** (2014) 361 - 369.

13. Kishore Sridharan, Milan Agarwal, Jacob Philip, Tamio Endo, Reji Philip, Trans. Mater. Res. Soc. Jpn. **35** (2010)159 - 162.
14. Shiji Krishnan, C.S. Suchand Sandeep, Reji Philip, Nandakumar Kalarikkal, Chem. Phys. Lett. **529** (2012) 59 - 63.
15. Sverre M Selbach, Mari-Ann Einarsrud, Thomas Tybell, Tor Grande, J.Am..Ceram.Soc. **90 (**2007) 3430 - 3434.
16. Manisha Arora, P.C Sati, Sunil Chuhan, Sandeep Chhoker, A.K Panwar, Manoj Kumar, J. Supercond. Nov. Magn. **26** (2013) 443 - 448.
17. S. Ghosh, S. Dasgupta, A. Sen, H.S. Maiti, J. Am. Ceram. Soc. **88** (2005)1349 - 1352.
18. Xiao Ying Guan, Zhong Wang Qiaoi, Deng Zhou Yani, Yan Fei Suni, Jin Li, J. Mater. Sci.: Mater. Electron **26** 6 (2015) 807 - 6813.
19. S. Li, Y. Lin, B. Zhang, Y. Wang, C.Nan, J.Phys. Chem. C **114** (2010) 2903 - 2908.
20. Cameliu Himcinschi, Ionela Vrejoiu, Marion Friedrich, Li Ding, Christoph Cobet, Norbert Esser, Marin Alexe, Dietrich R. T. Zahn, Phys. Stat. Sol. C **7** (2010) 296 - 299.
21. Xuelian Yu, Xiaoqiang An, Solid State Commun. **49** (2009) 711 - 714.
22. N. Miriyala, K. Prashanthi, T.Thundat, Phys. Stat. Sol. RRL **7** (2013) 668 - 671.
23. Vikash Singh, Subhash Sharma, R.K. Dwivedi, Manoj Kumar, R.K. Lotnala, Phys. Stat. Sol. A **210** (2013) 1442 - 1447.
24. I. Sosnowska, T.Peterlin-neumaier, E.Steichele, J. Phys. C: Solid State Phys.**15** (1982) 4835 - 4846.
25. Sanjay Godara, Nidhi Sinha, Geeta Ray, Binay Kumar, J. Asian Ceram. Soc. **2** (2014) 416 – 421.
26. M. Muneeswaran, P. Jegatheesan, M. Gopiraman, Ick-Soo Kim, N.V. Giridharan, Apply. Phys. A **114** (2014) 853 - 859.
27. Rajasree Das, Gobinda Gopal Khan, Kalyan Mandal, J. Appl. Phys. **111** (2012) 104115
29. Weiwei Hu, Yan Chen, Hongming Yuan, Guanghua Li,.
28. Amit Kumar, K. L. Yadav, Physica B **405** (2010) 4650 - 4654. Yu Qiao, Yuanyuan Qin, Shouhua Feng, J. Phys. Chem. C **115** (2011) 8869 - 8875.
30. Rajasree Das, Tanushree Sarkar, K.Mandal, J. Phys. D: Appl. Phys. **45** (2012) 455002.
31. J. Wu, J. Wang, D. Xiao, J. Zhu, Appl. Mater. Interfaces **4** (2012) 1182 - 1185.

32. J. Wu, S.Qiao, J. Wang, D. Xiao, J. Zhu, Appl. Phys. Lett. **102** (2013) 052904.
33. A. K Pradhan, Kai Zhang, D. Hunter, J.B Dadson, G.B Louts, J.Appl. Phys. **97 (**2005) 0939039.
34. C.G Koops, Phys. Rev. **83** (1951) 121 - 124.
35. D. Arun Kumar, S. Selvasekarapandian, H. Nithya, A. Sakunthala, M.Hema, Physica B **405** 2010) 3803 - 3807.
36. V.R Palkar, D.C Kundaliya, S.K Malik, S. Bhattacharya, Phys. Rev. B **69** (2004) 212102.
37. Robert W. Boyd, Nonlinear Optics, Rochester, New York, USA (2003) Chapt. 4.
38. Panit Chantharasupawong, Reji Philip, Tamio Endo, Jayan Thomas, Appl. Phys. Lett. **100 (**2012) 221108.
39. S. Abed, K. Bouchouit, M.S. Aida, S. Taboukhat, Z. Sofiani , B. Kulyk , V. Figa, Opt. Mater. **56** (2016) 10 - 14.
40**.** S. Abed, H. Bougharraf, K. Bouchouit, Z. Sofiani, B. Derkowska-Zielinska, M S. Aida, B. Sahraoui, Superlattices Microsrtuct. 85 (2015) 370 - 378.
41. K. Iliopoulos, A. El-Ghayoury, H. El Ouazzani, M. Pranaitis, E. Belhadj, E. Ripaud, M. Mazari, M. Sallé, D. Gindre, B. Sahraoui, Opt. Express **20** (2012) 25311 - 25316.
42. A. El-Bey, T. El Bahraoui, M. Taibi, A. Belayachi, A M.Abd-Lefdil1, A. M. El-Naggar, A.A.Albassam, A.O.Fedorchuk, G.Lakshminarayana, P.Czaja , I.V.Kityk, J. Alloys Compd. (accepted manuscript, doi:10.1016/j.jallcom.2016.05.130 (2016).

Acknowledgement

The authors sincerely thank the Department of Science and Technology (DST-FIST), Government of India for the instrumentation facilities.

Research Highlights

- Single phase $BiFeO_3$ nanoparticles by sol-gel method.
- Room temperature multiferroic properties.
- Verification of magnetic transition from dielectric analysis.
- Reverse saturable absorption (RSA) based optical limiting behavior with low limiting threshold.